MoO$_x$ thin films deposited by magnetron sputtering as an anode for aqueous micro-supercapacitors

Can Liu, Zhengcao Li and Zhengjun Zhang

The State Key Laboratory for New Ceramics and Fine Processing, School of Materials Science and Engineering, Tsinghua University, Beijing 100084, People's Republic of China

E-mail: zjzhang@tsinghua.edu.cn

Abstract

In order to examine the potential application of non-stoichiometric molybdenum oxide as anode materials for aqueous micro-supercapacitors, conductive MoO$_x$ films ($2 \leqslant x \leqslant 2.3$) deposited via RF magnetron sputtering at different temperatures were systematically studied for composition, structure and electrochemical properties in an aqueous solution of Li$_2$SO$_4$. The MoO$_x$ ($x \approx 2.3$) film deposited at 150 °C exhibited a higher areal capacitance (31 mF cm^{-2} measured at 5 mV s^{-1}), best rate capability and excellent stability at potentials below -0.1 V versus saturated calomel electrode, compared to the films deposited at room temperature and at higher temperatures. These superior properties were attributed to the multi-valence composition and mixed-phase microstructure, i.e., the coexistence of MoO$_2$ nanocrystals and amorphous MoO$_x$ ($2.3 < x \leqslant 3$). A mechanism combining Mo(IV) oxidation/reduction on the hydrated MoO$_2$ grain surfaces and cation intercalation/extrusion is proposed to illustrate the pseudo-capacitive process.

1. Introduction

Micro-electrochemical-capacitors (m-EC), or micro-supercapacitors, have attracted much attention as they can be integrated on a chip to power micro-electromechanical systems [1–4]. Selection and design of the electrode materials has proved crucial. Research efforts devoted to macro-ECs have shown that cheap, safe and environmentally friendly ECs having high power and energy densities could be produced by employing asymmetric electrode materials working within different potential windows in mild aqueous electrolytes [5–10]. This concept is also applicable to m-ECs [4]. Ruthenium oxide and manganese oxide have

been proved to be excellent candidates for cathode materials due to their high positive cutoff potential [11, 12]. However, anode materials are usually restricted to carbon materials, whose electrochemical performance is outstanding in strong acidic or alkaline aqueous electrolytes, but moderate in mild aqueous electrolytes, because of the lack of a pseudo-capacitive process [6, 7]. Although some work has been carried out on the development of oxide-based negative electrode materials, such as iron oxides, titania, tin and indium oxides [13–19], their properties are still not robust enough to compete with active carbon. Typically, active carbon shows a specific capacitance of over 80 F g^{-1} in mild aqueous solutions [10]. However, the volumetric capacitance, which is also an important characteristic for evaluating the charge-storage capacity of m-ECs [20], is unsatisfactory (55–180 F cm^{-3}) [2, 21, 22]. Besides, it is not convenient to directly integrate the active carbon powder onto

the film device [2]. Therefore, further research on thin-film materials as the pseudo-capacitive anode for m-Ecs is deemed necessary.

As a structurally diverse multi-valence compound, molybdenum oxides, including MoO_3, MoO_2 and MoO_x ($2 < x < 3$), have been considered as pseudo-capacitor electrode materials and investigated in various forms of nanostructures and nano-composites, where α-MoO_3 is most commonly studied due to its thermodynamic stability and orthorhombic layer structure [23–27]. However, the poor electrical conductivity and solubility in aqueous electrolyte restrict its further application in m-ECs. The Pourbaix diagram indicates that molybdenum oxides in valences lower than VI are stable in neutral or slightly acidic solutions at potentials below 0.3 V versus normal hydrogen electrode and have relatively high hydrogen overpotential [28]. Recently, Xiao *et al* [29] found that amorphous MoO_{3-x} layers (tens of nanometer thick) coated via electrodeposition exhibit an excellent performance as anodes of asymmetric supercapacitors. The layer is composed of Mo(VI) and Mo(V) and its equivalent resistance increases with thickness, which could lead to poor capability rate once a thicker film is prepared. Conductive MoO_2 has also been investigated as an anode material in rechargeable lithium batteries [30, 31]. The MoO_2 grains buried into a sub-stoichiometric film may reduce the resistance and improve the electrochemical performance. In this paper, highly conductive MoO_x films were prepared at different temperatures by sputtering MoO_3 under pure Ar atmosphere. The electrochemical properties in 0.5 M Li_2SO_4 solution have been investigated. The non-stoichiometric MoO_x films containing amorphous species and nanocrystals perform better than the purely amorphous structure or crystalline structure, indicating a possible candidate of anode materials for m-ECs. Meanwhile, the mechanism of the electrochemical process is discussed.

2. Experimental details

MoO_x films were deposited on FTO glass (SnO_2:F) via RF magnetron sputtering from a MoO_3 (99.95% purity) target, using a power of 105 W. The base pressure was below 3×10^{-4} Pa, and the sputtering pressure was 1 Pa in pure Ar atmosphere. The temperatures of the substrates were varied from room temperature (RT) to 350 °C, and each deposition lasted for 90 min. Here, RT means that the substrate was not intentionally heated during deposition, and the temperature detected by a thermocouple on the back of the sample stage was 50–60 °C, meaning that the substrate was naturally heated by the sputtering beam. In order to facilitate crystallization, the substrate was also heated from 150 to 350 °C during deposition.

The morphologies of the films were examined by field-emission scanning electron microscopy (SEM, JEOL-JMS-7001F) coupled with energy dispersive x-ray spectroscopy (EDS). The surface roughness was examined by a scanning probe microscopy system (SPI4000&SPA300HV) operated in the dynamic force microscopy mode. Inductively coupled plasma emission spectrometer (ELAN DRC-e) was

used to measure the Mo content so that the mass of the films could be calculated according to the atomic ratio of O/Mo. Film thicknesses were measured by a surface profiler. X-ray diffraction (XRD) patterns were acquired on a Rigaku x-ray diffractometer using Cu Kα radiation at 40 kV and 200 mA, in a continuous scan mode with a scan step of 0.02° in the range of 8–65°. Micro-Raman spectra were recorded using a LABRAM HR800 spectrometer equipped with a He–Ne laser ($\lambda = 632.8$ nm). The laser power was attenuated to 1 mW, focusing at a spot of 2 μm in diameter, so that laser irradiation effects such as oxidation or crystallization could be avoided.

The electrochemical measurements were carried out in a CHI660D electrochemical workstation connected to a typical three-electrode assembly in which a saturated calomel electrode (SCE) was used as reference electrode, a Pt foil as the counter electrode and a MoO_x/FTO sample as the working electrode. Li_2SO_4 aqueous solution (0.5 M) was selected as the electrolyte, whose pH was 4.1. All the electrochemical experiments were conducted under a freely aerated condition. Cyclic voltammetry (CV) was carried out down to −0.85 V versus SCE at rates of 5–100 mV s^{-1}. The electrochemical impedance spectra were recorded within the range of 0.01 Hz–0.5 MHz using a sinusoidal potential modulation of 5 mV.

3. Results and discussion

All the as-prepared films appeared opaque, silver gray and conductive. The film compositions were analyzed by EDS. Considering the film thicknesses (754–917 nm) and the detecting depth of EDS ($\sim$1 μm), it is understandable that signals of Sn and Si from the substrate also appeared in spectra; the total atomic concentrations of these elements were below 3%. The O content from the substrates was supposed to be proportional to Sn and Si contents according to the stoichiometry of SnO_2 and SiO_2, which were subtracted when calculating the O/Mo atomic ratio of the deposited films. As shown in table 1, the O/Mo atomic ratio in the films decreases from 2.3 to 2.0 when the deposition temperature increases. The Mo contents, masses, thicknesses and surface roughness of the films are also summarized. It is found that the masses and surface roughness (14–16 nm) are similar for all the samples. The thicknesses are close to each other for those deposited at 150–350 °C, while the film prepared at RT is thicker. This infers that the structure of the RT sample is much looser than that of the heated ones, probably containing more defects and voids. This is comprehensible since under a constant deposition rate, atoms gain higher energy to diffuse to stable sites so as to form a denser and more stable structure when the substrate temperature is elevated. This accords with the general film formation model of physical vapor deposition processes [32]. The density of the RT sample is estimated to be only about 4.9 g cm^{-3}, while that of the heated ones are 5.9–6.4 g cm^{-3}, close to the referenced data of 6.44 g cm^{-3} for MoO_2. Therefore, we conclude that the films are highly reduced MoO_x, with a composition closer to MoO_2 than MoO_3.

Table 1. Compositions and thicknesses of the MoO$_x$ films deposited at different temperatures.

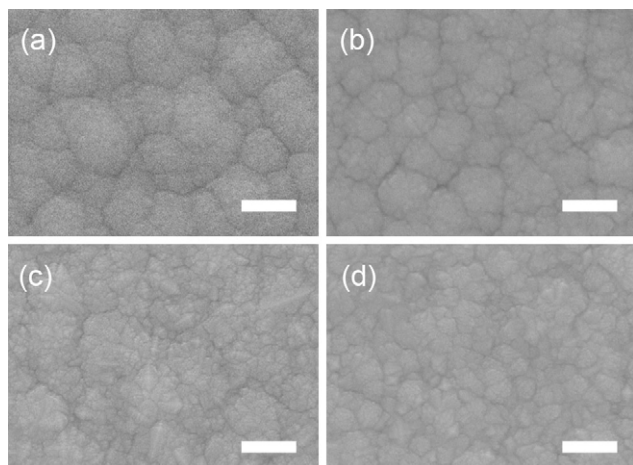| Deposition temperature (°C)	RT	150	200	250	300	350
O/Mo ratio	2.3	2.3	2.2	2.1	2.0	2.0
Mo content (μg cm^{-2})	328	351	331	355	359	356
Film mass (mg cm^{-2})	0.453	0.486	0.453	0.480	0.479	0.475
Film thickness (nm)	917	802	765	793	754	772
Surface roughness (nm)	14	14	15	14	16	15

Figure 1. Top-view SEM images of MoO$_x$ films deposited at (a) RT, (b) 150 °C, (c) 250 °C and (d) 350 °C. The scale bars represent 300 nm.

Figure 1 shows the top-view SEM images of the MoO$_x$ films prepared at different temperatures. All the films are flat and compact, evolving from featureless domains in the RT sample to homogeneously dispersed small crystal grains in the sample of 350 °C, with the gradual diminishing of domain boundaries. The evolution of the film morphology with the increase of deposition temperature could be explained by the zone structure model [32]. It is worth noting that the film of 150 °C (figure 1(b)) shows a compounded architecture containing both the domains ($\sim$200 nm) and crystal grains (tens of nanometers). The XRD patterns of the MoO$_x$ films and FTO glass are shown in figure 2(a). XRD result of the RT sample is similar to that of the FTO glass, indicating an amorphous film was obtained. Other spectra exhibit diffraction peaks indexed to monoclinic MoO$_2$ (JCPDS: 78-1073, m-MoO$_2$), illustrating crystallized MoO$_2$ present in the films when the deposition temperature is above 150 °C. For detailed comparison, a slow scan (scanning rate: 1° min^{-1}, step: 0.1°) around (−112) diffraction of m-MoO$_2$ was conducted, with K-α_2 radiation screened out, as shown in figure 2(b). When the temperature increases from 150 to 300 °C, the intensity increases while the peak width decreases. A peak shift toward lower diffraction angle for 150 and 200 °C is also observed. Crystallite size could be estimated according to the Scherrer's equation, $D = K\lambda / B \cos \theta$, wherein D is the crystal size at the direction normal to the diffraction plane, K is the Scherrer constant which was taken as 0.89, λ is the wavelength of x-ray (0.15 406 nm), B is the full width at half maximum and θ is the diffraction angle [33]. Calculations indicate that the crystal size increases from
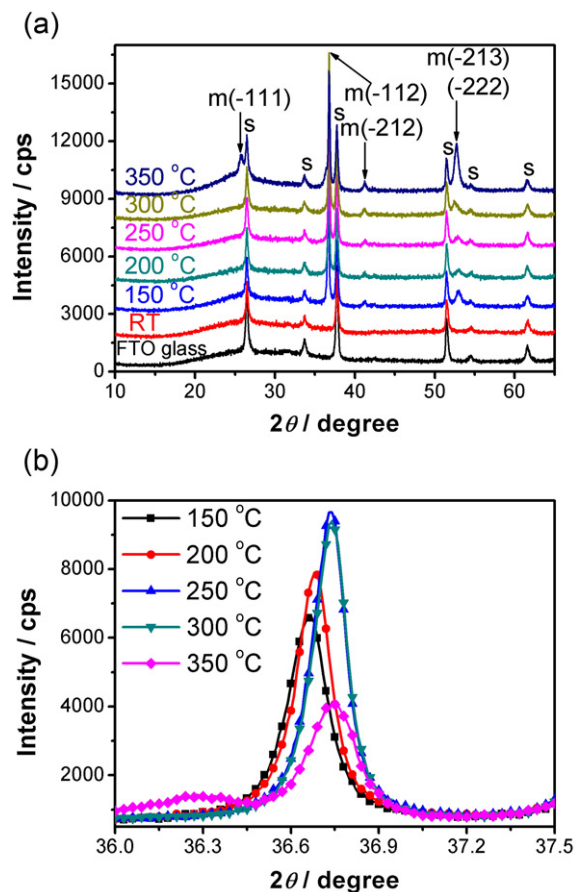
Figure 2. (a) XRD patterns of FTO glass and MoO$_x$/FTO samples prepared at RT and 150–350 °C, wherein s represents the diffraction peaks of FTO and m stands for monoclinic MoO$_2$ (JCPDS: 78-1073); (b) fine XRD spectra around the (−112) diffraction of monoclinic-MoO$_2$ for the MoO$_x$/FTO samples prepared at 150–350 °C.

47 to 57 nm as temperature increases from 150 to 300 °C, coinciding with the crystal size shown in figure 1. Peak shifts for the samples of 150 and 200 °C suggest the existence of tensile stress. As to the sample of 350 °C, other peaks emerge at the cost of weakening the (−112) peak. The widening of this diffraction peak could be attributed to the exposing of (−2 − 11) and (020) peaks which are only 0.08° and 0.16° away from (−112), respectively. And this implies the diminishing of a certain texture at 350 °C, which is in agreement with the nearly equiaxed grain morphology shown in figure 1(d). Therefore, it could be deduced that more and more MoO$_2$ grains form, grow and become more crystallized when deposition temperature increases from 150 to 350 °C. Furthermore, regarding the O/Mo ratios for the films of
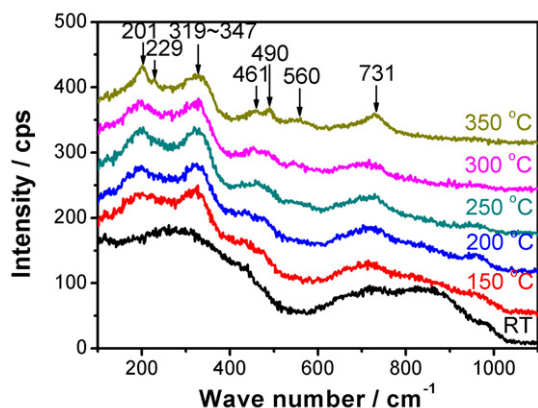
Figure 3. Raman spectra of MoO$_x$ films deposited at RT and 150–350 °C.

150–250 °C in table 1, it is supposed that there are other species present with an amorphous structure, whose O/Mo ratio should be higher than 2, e.g. amorphous MoO$_3$.

Figure 3 shows the Raman spectra of these MoO$_x$ films. Consistent with the XRD result, only ague heaves are observed in the spectrum for the RT sample, indicating a thoroughly amorphous structure. A series of envelopes starts to appear at 150 °C, and evolve into distinct peaks when the deposition temperature is raised to 350 °C. This illustrates that enhancing deposition temperature is favorable for better crystallization. The Raman bands in figure 3 further confirm the existence of monoclinic MoO$_2$ as a main component for samples produced above 150 °C [34, 35]. The broadening of the Raman bands in the films of 150–300 °C may be due to their small grain sizes which are estimated by XRD to be only tens of nanometers. In addition, a bump between 800 and 1000 cm^{-1} on the curve of the RT sample and another near 1000 cm^{-1} are found for samples of 150–250 °C. The latter is considered to be the characteristic vibrations of MoO$_3$ [36]. This further confirms that a highly oxidized and non-crystalline species, probably MoO$_3$, exists in the MoO$_x$ films of RT ∼ 250 °C. Therefore, it could be concluded that different components of MoO$_x$ films were attained when the deposition temperature increased: an amorphous sub-stoichiometric (MoO$_{2.3}$) film at RT, a multi-valence and mixed-phase film containing both MoO$_2$ grains with (−112) texture and amorphous MoO$_x$ ($x > 2$) at 150–250°, and an almost pure crystalline MoO$_2$ film at 300–350 °C.

Figures 4(a) and (b) show CV results of these MoO$_x$/FTO films, at scan rates of 50 and 5 mV s^{-1}, respectively. The nearly rectangular and symmetric shape of the CV curves at 50 mV s^{-1} illustrates certain capacitive behavior in aqueous electrolyte. For the RT sample, the CV curve has a more ideal shape, similar to the CV characteristic of the hydrated amorphous MoO$_{(3−x)}$ prepared by electrodeposition [29, 37]. However, the current tends to diminish at the potentials above −0.2 V, with the shape of the curve evolving into a triangular shape (figure 4(b)). As the test goes on, the film easily deteriorates. For the other samples, the CV curves resemble each other but shrink as the deposition temperature increases, and peaks (or partial peaks) could be observed at the potentials above −0.2 V and below −0.6 V, respectively.
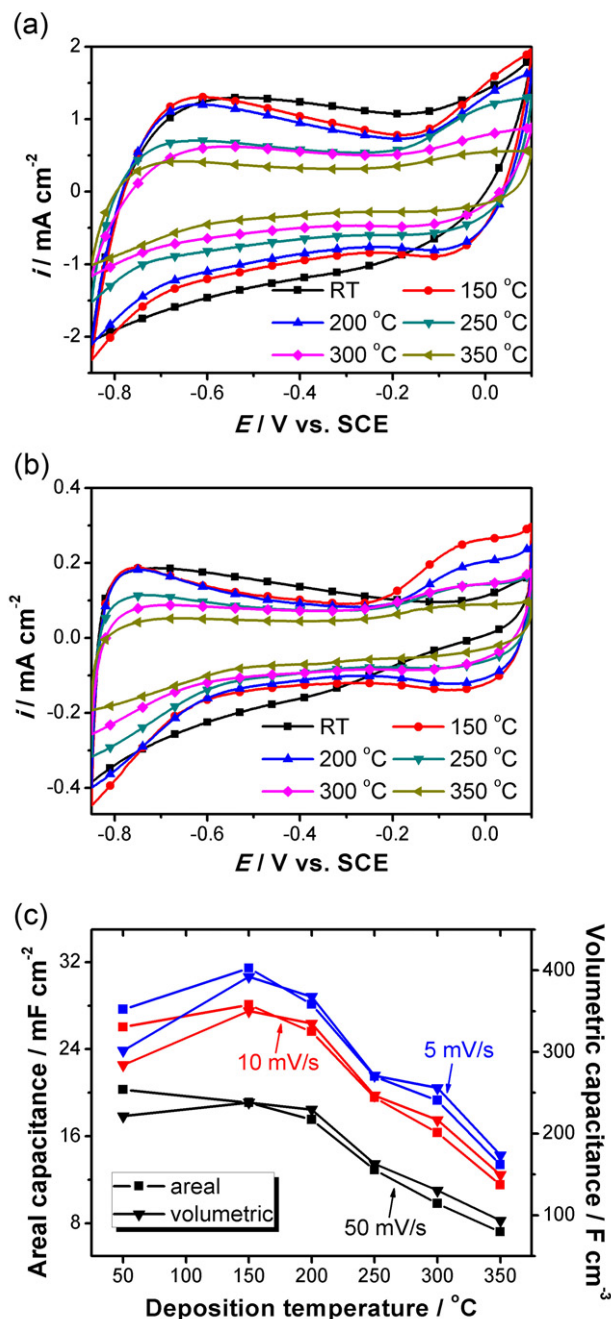

Figure 4. CV curves of MoO$_x$/FTO samples deposited at RT and 150–350 °C, acquired at a scan rate of (a) 50 mV s^{-1} and (b) 5 mV s^{-1} in 0.5 M Li$_2$SO$_4$ aqueous solution. (c) The areal capacitances and volumetric capacitances for the MoO$_x$/FTO samples deposited at RT and 150–350 °C, estimated from CV curves. The data points of 50 °C correspond to the sample of RT.

CV measurements were also carried out at different sweep rates. The corresponding areal capacitances (normalized by apparent area) and volumetric capacitances (normalized by volume) are evaluated. For each sample, the capacitance monotonically increases when the scan rate is reduced. For a clear comparison among the samples, the capacitances measured at 5, 10 and 50 mV s^{-1} are summarized in figure 4(c). Since the surface roughness is close to each other (see table 1), it is reasonable to adopt the apparent geometric area to estimate the areal capacitance.
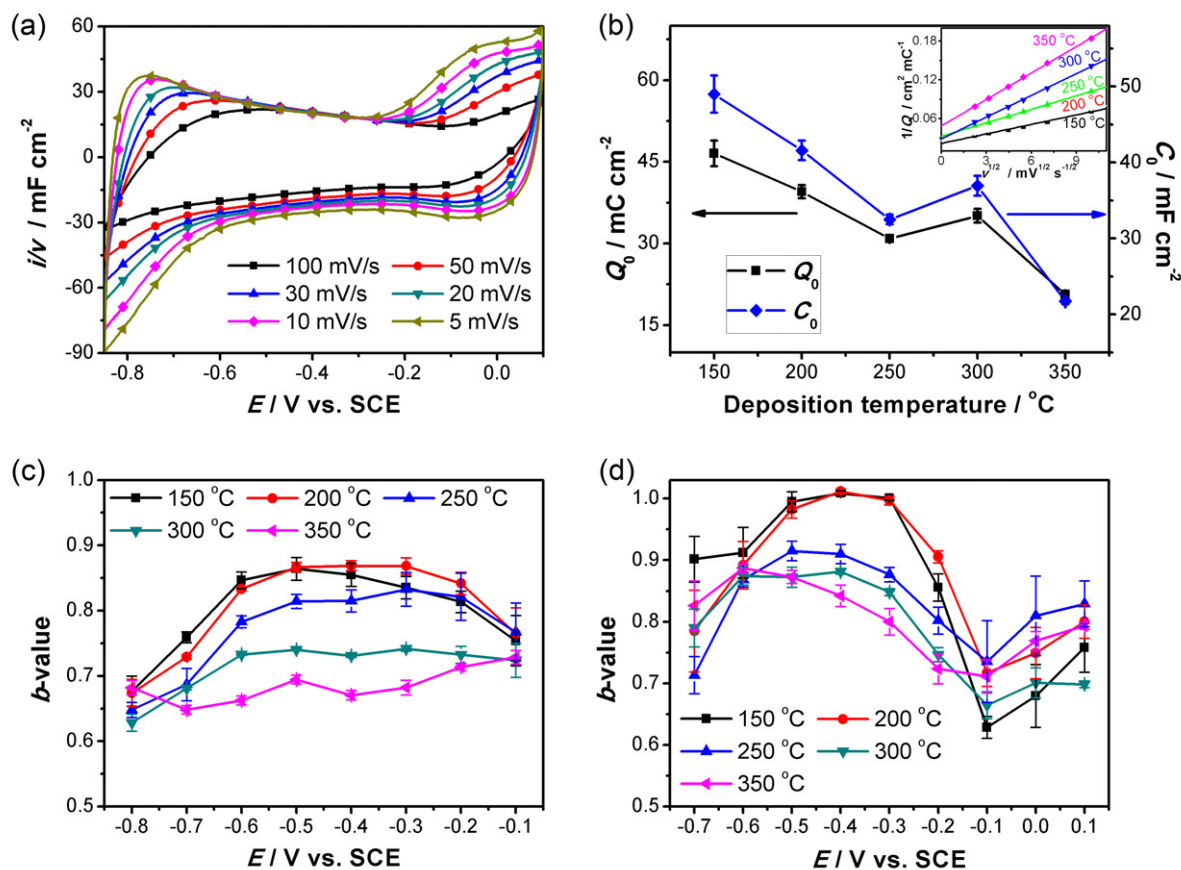
Figure 5. (a) CV curves for the MoO$_x$/FTO film deposited at 150 °C scanned at rates differing from 100 to 5 mV s^{-1}, on which the vertical axis is transferred into differential capacitance derived from dividing current density i by sweep rate v. (b) Charge limit Q_0 and capacitance limit C_0 for the MoO$_x$/FTO films prepared at 150–350 °C, derived from extrapolation to $v = 0$. Inset: linear fittings of $1/Q$ versus $v^{1/2}$ for the films of 150–350 °C, wherein Q represents charge capacity of each CV cycle. (c) b-values for the films of 150–350 °C plotted as a function of potential for cathodic sweeps. (d) b-values for the films of 150–350 °C plotted as a function of potential for anodic sweeps.

Although the areal capacitance of the RT film is a bit higher than that of the 150 °C at 50 mV s^{-1}, it becomes lower than the latter in the later measurement at 10 and 5 mV s^{-1} because of the irreversible deterioration. At each scan rate, the areal capacitance decreases with the increase of deposition temperature from 150 to 350 °C. A similar monotonous decreasing relation was observed between volumetric capacitance and deposition temperature.

In terms of application, the highest areal capacitance, i.e. 31 mF cm^{-2} measured at 5 mV s^{-1}, is achieved by the film of 150 °C. It is superior to other pseudocapacitive films under study as the anode, e.g. VN ($\sim$15 mF cm^{-2}) [4], and is also comparable to the reported cathode electrodes, e.g. manganese oxide and ruthenium oxide films (17–38 mF cm^{-2}) [38–40]. The corresponding specific capacitance normalized to mass is 65 F g^{-1} for this film. Although the gravitational capacitance is not high compared to those widely investigated materials, the volumetric capacitance is attractive for application in micro-devices. The film deposited at 150 °C also exhibits high volumetric capacitance, with the highest value of 392 F cm^{-3} at 5 mV s^{-1}. It maintains 309 F cm^{-3} at 20 mV s^{-1}, and 183 F cm^{-3} at 100 mV s^{-1}. These values are superior to that of carbide-derived-carbon films (160 F cm^{-3} measured at 20 mV s^{-1} in H$_2$SO$_4$ solution) [2] and single-walled

carbon nanotube films ($\sim$75 F cm^{-3} in H$_2$SO$_4$ solution) [21], implying that such MoO$_x$ could indeed be available as the anode material in aqueous m-ECs.

It is suggested that the capacitance of such MoO$_x$ films should not only originate from the double layer effect but also from the pseudo-capacitive effect. Double layer capacitance, which is contributed by electrostatically stored charge on the surface, is only related with the contacting area between the active material and the electrolyte [41, 42]. However, the pseudo-capacitance originates from the Faradaic charge-transfer process, which takes place within a certain subsurface layer. The thickness of the subsurface layer is determined by the penetration depth of the ions [41]. Therefore, the pseudo-capacitance property lies on the structure and orientation of the active material [43]. The relation between the areal capacitance and deposition temperature reflects the effect of microstructure on the pseudo-capacitance. In addition, the presence of the peaks in the CV curves of the crystallized samples deposited at 150–350 °C and the absence on that of the amorphous RT sample (see figure 4(a)) also support this inference.

For further analysis, the CV curves of the 150 °C sample at sweep rates from 5 to 100 mV s^{-1} are plotted in figure 5(a) as differential capacitance versus potential. The differential

capacitance is defined as the ratio of density i to the sweep rate v. Obviously, there are three different sections: in the middle section, i.e. -0.5 to -0.3 V, the differential capacitance is almost irrelevant to v, indicating a capacitive process; in the other two sections, i.e. the regions below -0.5 V and above -0.3 V, the differential capacitance has an inverse relationship to v, implying diffusion-controlled processes.

In order to evaluate the rate capability and charge limits, we examined the relation between the charge capacity Q and the scan rate v, based on the Trasatti method [44]. In this approach, Q is inversely proportional to $v^{1/2}$. Thus, a linear equation is assumed as $1/Q = 1/Q_0 + \text{const}^*\sqrt{v}$, and the capacity limit Q_0 could be obtained through extrapolation to $v = 0$. The slope reflects the rate capability: lower slope indicates better rate capability. Linearity is excellent for all these samples, as shown in the inset of figure 5(b). The slopes of the fitting lines increase with deposition temperature, indicating that the diffusion-controlled process becomes predominant as the film becomes more crystallized. The 150 °C sample exhibits the best rate capability in our study. Q_0 and the corresponding capacitance limit C_0 are plotted against the deposition temperature in figure 5(b). It was found that Q_0 decreases roughly as deposition temperature increases and the film of 150 °C shows the highest upper limit of the achievable capacity. This may be explained as its special structure, combining more amorphous MoO_x (x approaches 3) and poorer crystallized MoO_2 grains, permits ions to diffuse deeper into the material and facilitate the charge transfer. The upper limit of areal capacitance for the 150 °C film, i.e. 49 mF cm^{-2}, could be translated to a volumetric value of 611 F cm^{-3}. The reverse relation between Q_0 of the 250 and 300 °C samples may be attributed to the real surface area difference, however, the exact factor is still unclear.

The capacitive effects throughout the potential range were further characterized by employing a power law relation between current density i and sweep rate v: $i = av^b$, wherein a and b are adjustable parameters [45]. $b = 0.5$ refers to the direct proportion between i and $\sqrt{v}$ following the semi-infinite diffusion model; $b = 1$ corresponds to a pure capacitive response, i.e. $i = vC$, in which C is the areal capacitance. The experimental data can be linearized as $\ln(i)$ versus $\ln(v)$ indeed, and the resulting b-values in cathodic sweeps and anodic sweeps for the films of 150–350 °C are plotted in figures 5(c) and (d), respectively. The relatively low b-values at -0.8 V in cathodic sweeps (see figure 5(c)) and at -0.1 V in anodic sweeps (see figure 5(d)) indicate diffusion-controlled process for all the films of 150–350 °C. It is reasonable to suggest that the process occurs around -0.1 V in anodic sweep is participated by crystalline MoO_2 grains, considering the lack of anodic peak in the amorphous RT sample (see figures 4(a) and (b)). From figure 5(c), it is found that the b-values of the 300 and 350 °C samples are small within the whole potential range, which means a diffusion-controlled process onto the grains or grain boundaries exists throughout the entire cathodic sweep. It is also obvious that the b-values of the 150 and 200 °C samples are extraordinarily higher than those of the 300 and 350 °C samples from -0.6 to -0.3 V. A similar phenomenon in anodic sweeps could be seen from
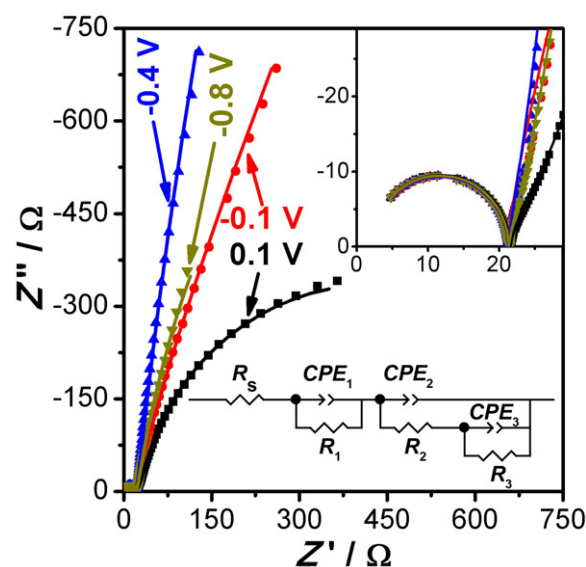

Figure 6. EIS Nyquist plots at 0.1, -0.1, -0.4 and -0.8 V for the film deposited at 150 °C, in which the scattered spots represent experimental data and the solid lines are simulated curves. Inset at the top right corner: the enlarged high frequency region of the EIS plots. Inset at the bottom right corner: the equivalent circuit model used for simulation. The circuit element CPE refers to constant phase element, which is in place of a capacitor to compensate for non-homogeneity in the system.

figure 5(d). As an explanation, the amorphous MoO_x species in the 150 and 200 °C films probably participated in the process from -0.6 to -0.3 V, contributing capacitive current. The high current density at $-0.6 \sim -0.3$ V for the RT sample even after certain deterioration (see figure 4(b)) also agrees with this inference.

In order to further investigate the electrochemical process, the electrochemical impedance spectroscopy (EIS) was also carried out. Figure 6 displays the Nyquist plots of the 150 °C sample, taken at potentials of 0.1, -0.1, -0.4 and -0.8 V, respectively. The spectra show similar characteristics in the high frequency section (see the top right inset in figure 6), but different in the low frequency region. The straight lines with slopes close to 90° along the imaginary axis (Z'') at the potential of -0.4 V corroborate the capacitive features revealed on CV [46]. Although it has been discerned from previous analysis that partially diffusion-controlled processes take place at -0.8 and -0.1 V, the straight lines with large slopes instead of Faradaic semi-circles in the low frequency spectra suggest that the charge transfer processes should be limited on the surface or a thin subsurface layer of the MoO_2 grains. For the spectrum at 0.1 V, there is a semi-circle conveying a dominant Faradaic redox reaction, reflecting dramatic oxidation. Hence, the upper potential limit should not exceed 0.1 V versus SCE. An equivalent circuit model was also constructed as shown in the inset of figure 6. The left part of the circuit, i.e. R_s(CPE$_1$ R_1), represents the impedance contributed by the substrate. The right part is a model of typical electrochemical system containing pseudo-capacitances [47]. The fitting parameters are listed in table 2, validating excellent consistency between the proposed model and experimental data (figure 6).

Table 2. Simulating parameters of the equivalent model in figure 6 for the EIS data at 0.1, −0.1, −0.4 and −0.8 V for the MoO_x/FTO film deposited at 150 °C. The impedance of CPE is $Z = 1/[T(i\omega)^P]$, wherein T is the capacitance when $P = 1$, and P is the constant phase exponent ($0 \leqslant P \leqslant 1$).

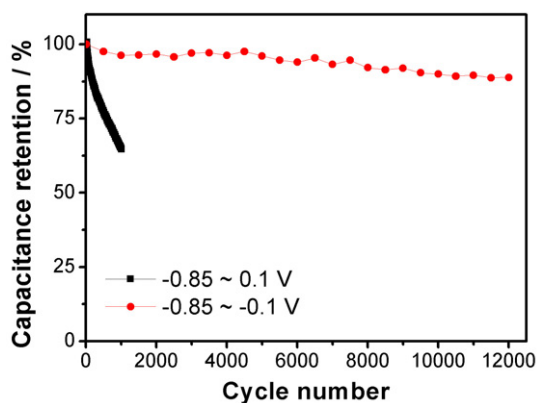| Potential (V)	R_s (Ω)	CPE_1-T (10^{-8} F)	CPE_1 P	R_1 (Ω)	$CPE_2 - T$ (F)	CPE_2-P	R_2 (Ω)	CPE_3-T (F)	CPE_3-P	R_3 (kΩ)	χ^2 (10^{-4})
0.1	2.1	7.80	0.99	19.5	0.011	0.88	35	0.008	0.90	0.77	8.7
−0.1	2.4	7.40	0.99	18.9	0.011	0.95	88	0.004	0.65	35	6.7
−0.4	2.2	7.60	0.99	19.1	0.017	0.92	309	0.001	1.01	25	5.7
−0.8	2.1	7.40	0.99	19.2	0.028	0.90	71	0.005	0.91	3.4	7.2

Figure 7. Capacitance retention for the MoO_x films deposited at 150 °C during CV cycling at 20 mV s^{-1}, within the potential windows of −0.85 to 0.1 V and −0.85 to −0.1 V.

Figure 7 shows the cycling stability of the MoO_x films deposited at 150 °C within the potential ranges of −0.85 to 0.1 and −0.85 to −0.1 V. The stability within −0.85 to 0.1 V is not satisfying, i.e. only 65% of the initial capacitance is retained after 1013 cycles. However, if the upper potential limit is lowered to the initial open circuit potential of −0.1 V, excellent stability is maintained, with 97% of the capacitance retained after 2000 cycles and 89% retained after 12 000 cycles. Aforementioned EIS analysis suggests that dramatic oxidation takes place at 0.1 V. According to the Pourbaix diagram, soluble MoO_4^{2-} is the stable phase at 0.1 V versus SCE in the present pH condition [28]. Thus it is conjectured that oxidation of MoO_2 grains at 0.1 V leads to dissolution and causes deterioration during long term cycling. In terms of application, the upper limit of −0.1 V versus SCE is also acceptable for asymmetric supercapacitors, since positive electrodes based on MnO_2 could work in a potential range down to −0.1 V versus SCE [17]. Furthermore, the upper potential limit could be further extended, for example, by covering a carbon layer on the MoO_x film, as was proposed in the literature to protect $LiTi_2(PO_4)_3$ from dissolution [16].

There are few reports on the electrochemical behavior of substoichiometric molybdenum oxides in aqueous solution. According to the Pourbaix diagram, MoO_2 is stable below −0.4 V versus SCE in mild Li_2SO_4 solution, hence valence change within the bulk MoO_2 grains could be neglected below −0.4 V, which has been confirmed in early studies where Li^+ intercalation into MoO_2 happens below 2.0 V versus Li/Li^+, i.e. below −1.3 V versus SCE [28, 30, 31]. Hydrogen evolution should be basically ruled out in our

case, because no bubbles have ever been observed during the tests. Furthermore, the CVs are nearly reversible, and the impedance spectra at −0.85 V still reflect capacitive characteristics for all the samples. Nevertheless, H^+ ions may be involved in the process by reversible adsorption/desorption to the amorphous MoO_x species and the MoO_2 grain surfaces, which is discussed below.

The Pourbaix diagram tells us that MoO_2 would be oxidized into soluble MoO_4^{2-} above −0.4 V, but we suspect that the oxidation depends on the specific structure of MoO_2. Horkans and Shafer [48] have shown that anodic dissolution for single crystalline MoO_2 happens above ∼0.65 V in 1 N H_2SO_4 solution, which is ∼0.4 V higher than the potential given by the Pourbaix diagram [28]. In our study, the amorphous MoO_x film of RT indeed exhibits continually diminishing loops at the higher potential region, i.e. −0.3 to 0.1 V versus SCE. The Faradaic feature appears at the potential as low as −0.1 V in the EIS spectra (not shown here). This behavior is consistent with the Pourbaix diagram. However, for the films deposited at 150–350 °C which contains crystalline MoO_2, Faradaic semi-circles only exist at potentials as high as 0.1 V in the EIS spectra (see figure 6). This may indicate that significant oxidation of bulk MoO_2 grains starts above 0.1 V, which is also in agreement with the implication from the cycling test results discussed previously. Thus the broad peaks around −0.1 V in the CV curves may suggest a reversible oxidation reaction on the hydrated surfaces of MoO_2 grains following the mechanisms such as $MoO_2 \cdot yH_2O - \delta e^- \leftrightarrows MoO_2(OH)_\delta \cdot (y - \delta)H_2O + \delta H^+$. When the surfaces of the MoO_2 grains are hydrated and oxidized, cations will intercalate into this layer during cathodic sweeps, as shown in the following reversible reaction equations like $MoO_2(OH)_\delta \cdot (y - \delta)H_2O + \delta H^+ + \delta e^- \leftrightarrows MoO_2 \cdot yH_2O$. For the films deposited at 150–250 °C, the amorphous $MoO_x (x > 2)$ components in the films are easily hydrated and could accommodate inserted cations during cathodic sweeps, as the equations show $MoO_x \cdot yH_2O + \delta H^+ + \delta e^- \leftrightarrows MoO_{x-\delta}(OH)_\delta \cdot yH_2O$, $MoO_x \cdot yH_2O + \delta Li^+ + \delta e^- \leftrightarrows Li_\delta MoO_x \cdot yH_2O$ [24, 27, 49–51]. These reversible processes provide an extra contribution to the capacitance.

Based on this mechanism, the superior pseudo-capacitive performance of the film deposited at 150 °C over that of the samples with higher deposition temperatures could be attributed to its larger amount of amorphous $MoO_x (x > 2)$ component which facilitates hydration and provides more intercalation capacitance, and probably more hydrated MoO_2

grain boundaries as well, which promotes reversible surface oxidation/reduction of Mo(IV). In addition, as revealed by Song *et al* [52] on a mixed-valence manganese oxide film with mixed phases, the coexistence of aliovalent cations (Mo^{4+}, Mo^{5+} or Mo^{6+} here) may facilitate the formation of more ionic defects and electronic defects. Such a case may accelerate the kinetics of the surface charge transfer. Thus, the higher activity of the grain boundaries could also improve the capacitive property of the MoO_x film of $150\,^{\circ}$C.

4. Conclusions

Herein, we have prepared conductive MoO_x ($2 \leqslant x \leqslant 2.3$) films at temperatures from RT to $350\,^{\circ}$C by RF magnetron sputtering, and systematically investigated the electrochemical properties between -0.85 and $0.1\,$V versus SCE in $0.5\,$M Li_2SO_4 aqueous electrolyte. The effect of composition and microstructure on the electrochemical property is discussed. It was found that the $MoO_x (x \approx 2.3)$ film deposited at $150\,^{\circ}$C contains MoO_2 nanocrystals and amorphous MoO_x ($2 < x \leqslant 3$) species, and performs better than the films deposited at RT and temperatures above $150\,^{\circ}$C, with highest capacitance ($31\,$mF cm^{-2}, or $392\,$F cm^{-3} normalized by volume, measured at $5\,$mV s^{-1}), best rate capability and excellent cycling stability below $-0.1\,$V versus SCE, suggesting a suitable candidate for anode material in aqueous m-ECs. Such superior electrochemical performance could be attributed to its unique multi-valence composition and mixed-phase microstructure. A mechanism including oxidation/reduction on the hydrated MoO_2 grains surfaces and cation intercalation/extrusion below $-0.3\,$V is proposed to explain the pseudo-capacitive behavior of the MoO_x films. Nevertheless, further investigation is still needed to examine this mechanism. For example, the effect of electrolyte on the electrochemical process could be investigated so as to distinguish which ions play an active role. The dynamic features of the surface reactions mentioned above also need quantitative study, and whether a critical thickness of the active subsurface layer exists or not should be clarified. It is believed that knowledge about the electrochemical mechanism will help us to design outstanding thin film electrode materials for m-ECs in the future. Further optimization of the deposition condition is still needed to improve the electrochemical properties of these MoO_x films, which are under investigation.

Acknowledgments

References

[1] Pech D, Brunet M, Durou H, Huang P, Mochalin V, Gogotsi Y, Taberna P-L and Simon P 2010 *Nature Nanotechnol.* **5** 651

[2] Chmiola J, Largeot C, Taberna P-L, Simon P and Gogotsi Y 2010 *Science* **328** 480

[3] Heon M *et al* 2011 *Energy. Environ. Sci.* **4** 135

[4] Eustache E, Frappier R, Porto R L, Bouhtiyya S, Pierson J-F and Brousse T 2013 *Electrochem. Commun.* **28** 104

[5] Simon P and Gogotsi Y 2008 *Nature Mater.* **7** 845

[6] Wu Z-S, Ren W, Wang D-W, Li F, Liu B and Cheng H-M 2010 *ACS Nano* **4** 5835

[7] Lokhande C D, Dubal D P and Joo O-S 2011 *Curr. Appl. Phys.* **11** 255

[8] Zhang J, Jiang J, Li H and Zhao X S 2011 *Energy. Environ. Sci.* **4** 4009

[9] Yuan C-Z, Gao B and Zhang X-G 2007 *J. Power Sources* **173** 606

[10] Long J W, Belanger D, Brousse T, Sugimoto W, Sassin M B and Crosnier O 2011 *MRS Bull.* **36** 513

[11] Jow T R and Zheng J P 1998 *J. Electrochem. Soc.* **145** 49

[12] Patel M N, Wang X, Slanac D A, Ferrer D A, Dai S, Johnston K P and Stevenson K J 2012 *J. Mater. Chem.* **22** 3160

[13] Sassin M B, Mansour A N, Pettigrew K A, Rolison D R and Long J W 2010 *ACS Nano* **4** 4505

[14] Brousse T and Belanger D 2003 *Electrochem. Solid State Lett.* **6** A244

[15] Ng K C, Zhang S, Peng C and Chen G Z 2009 *J. Electrochem. Soc.* **156** A846

[16] Luo J-Y and Xia Y-Y 2009 *J. Power Sources* **186** 224

[17] Jin W-H, Cao G-T and Sun J-Y 2008 *J. Power Sources* **175** 686

[18] Santos-Pena J, Crosnier O and Brousse T 2010 *Electrochim. Acta* **55** 7511

[19] Chang J, Lee W, Mane R S, Cho B W and Han S-H 2008 *Electrochem. Solid State Lett.* **11** A9

[20] Wang K, Zou W, Quan B, Yu A, Wu H, Jiang P and Wei Z 2011 *Adv. Energy Mater.* **1** 1068

[21] Kaempgen M, Chan C K, Ma J, Cui Y and Gruner G 2009 *Nano Lett.* **9** 1872

[22] Chimola J, Yushin G, Gogotsi Y, Portet C, Simon P and Taberna P L 2006 *Science* **313** 1760

[23] Liang R L, Cao H Q and Qian D 2011 *Chem. Commun.* **47** 10305

[24] Tang W, Liu L L, Tian S, Li L, Yue Y B, Wu Y P and Zhu K 2011 *Chem. Commun.* **47** 10058

[25] Liu C, Li Z C and Zhang Z J 2011 *Appl. Phys. Lett.* **99** 223104

[26] Shakir I, Shahid M, Yang H W and Kang D J 2010 *Electrochim. Acta* **56** 376

[27] Saji V S and Lee C W 2012 *ChemSusChem* **5** 1146

[28] Pourbaix M 1974 *Atlas of Electrochemical Equilibria in Aqueous Solutions* (Brussels: National Association of Corrosion Engineers)

[29] Xiao X *et al* 2012 *Adv. Energy Mater.* **2** 1328

[30] Yang L C, Gao Q S, Zhang Y H, Tang Y and Wu Y P 2008 *Electrochem. Commun.* **10** 118

[31] Liang Y G, Yang S J, Yi Z H, Sun J T and Zhou Y H 2005 *Mater. Chem. Phys.* **93** 395

[32] Harsha K S S 2006 *Principles of Vapor Deposition of Thin Films* (Amsterdam: Elsevier)

[33] Cullity B D 1978 *Elements of X-Ray Diffraction* (Reading, MA: Addison-Wesley)

[34] Camacho-Lopez M A, Escobar-Alarcon L, Picquart M, Arroyo R, Cordoba G and Haro-Poniatowski E 2011 *Opt. Mater.* **33** 480

[35] Dieterle M and Mestl G 2002 *Phys. Chem. Chem. Phys.* **4** 822

[36] Spevack P A and McIntyre N S 1992 *J. Phys. Chem.* **96** 9029

[37] Li G R, Wang Z L, Zheng F L, Ou Y N and Tong Y X 2011 *J. Mater. Chem.* **21** 4217

[38] Nagarajan N, Humadi H and Zhitomirsky I 2006 *Electrochim. Acta* **51** 3039

[39] Wu M S 2005 *Appl. Phys. Lett.* **87** 153102

[40] Liu C-C, Tsai D-S, Susanti D, Yeh W-C, Huang Y-S and Liu F-J 2010 *Electrochim. Acta* **55** 5768

[41] Conway B E, Birss V and Wojtowicz J 1997 *J. Power Sources* **66** 1

[42] Brezesinski T, Wang J, Tolbert S H and Dunn B 2010 *Nature Mater.* **9** 146

[43] Zheng J P, Jow T R, Jia Q X and Wu X D 1996 *J. Electrochem. Soc.* **143** 1068

[44] Ardizzone S, Fregonara G and Trasatti S 1990 *Electrochim. Acta* **35** 263

[45] Wang J, Polleux J, Lim J and Dunn B 2007 *J. Phys. Chem. C* **111** 14925

[46] Sugimoto W, Iwata H, Yokoshima K, Murakami Y and Takasu Y 2005 *J. Phys. Chem. B* **109** 7330

[47] Conway B E 1991 *J. Electrochem. Soc.* **138** 1539

[48] Horkans J and Shafer M W 1977 *J. Electrochem. Soc.* **124** 1196

[49] Farsi H, Gobal F, Raissi H and Moghiminia S 2010 *J. Solid State Electrochem.* **14** 643

[50] McEvoy T M and Stevenson K J 2004 *J. Mater. Res.* **19** 429

[51] Gorenstein A, Lourenco A and Scarminio J 1996 *J. Electrochem. Soc.* **143** 2822

[52] Song M-K *et al* 2012 *Nano Lett.* **12** 3483